



Facile preparation of $[\text{Bi}_6\text{O}_4](\text{OH})_4(\text{NO}_3)_6 \cdot 4\text{H}_2\text{O}$, $[\text{Bi}_6\text{O}_4](\text{OH})_4(\text{NO}_3)_6 \cdot \text{H}_2\text{O}$ and $[\text{Bi}_6\text{O}_4](\text{OH})_4(\text{NO}_3)_6 \cdot \text{H}_2\text{O}/\text{C}$ as novel high capacity anode materials for rechargeable lithium-ion batteries

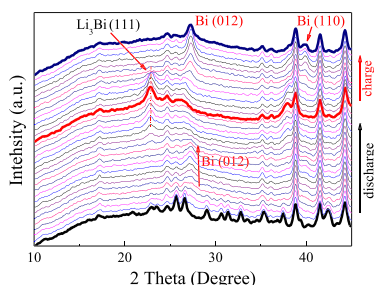
Kaiqiang Wu, Lianyi Shao, Xinxin Jiang, Miao Shui, Rui Ma, Mengmeng Lao, Xiaoting Lin, Dongjie Wang, Nengbing Long, Yuanlong Ren, Jie Shu*

Faculty of Materials Science and Chemical Engineering, Ningbo University, Ningbo 315211, Zhejiang Province, People's Republic of China

HIGHLIGHTS

- Facile preparation of basic bismuth nitrates as novel anode materials.
- Basic bismuth nitrates show an initial discharge capacity of $2792.9 \text{ mAh g}^{-1}$.
- The lithiation process of basic bismuth nitrates is partially reversible.

GRAPHICAL ABSTRACT



ARTICLE INFO

Article history:

Received 7 October 2013

Received in revised form

25 December 2013

Accepted 30 December 2013

Available online 4 January 2014

Keywords:

Lithium-ion batteries

Anode material

Basic bismuth nitrate

Electrochemical properties

ABSTRACT

$[\text{Bi}_6\text{O}_4](\text{OH})_4(\text{NO}_3)_6 \cdot 4\text{H}_2\text{O}$, $[\text{Bi}_6\text{O}_4](\text{OH})_4(\text{NO}_3)_6 \cdot \text{H}_2\text{O}$ and $[\text{Bi}_6\text{O}_4](\text{OH})_4(\text{NO}_3)_6 \cdot \text{H}_2\text{O}/\text{C}$, derived from $\text{Bi}(\text{NO}_3)_3 \cdot 5\text{H}_2\text{O}$, are firstly investigated for the electrochemical activity as anode materials for lithium-ion batteries. Electrochemical results show that $[\text{Bi}_6\text{O}_4](\text{OH})_4(\text{NO}_3)_6 \cdot 4\text{H}_2\text{O}$ can deliver a higher initial discharge specific capacity ($2792.9 \text{ mAh g}^{-1}$) than that of $[\text{Bi}_6\text{O}_4](\text{OH})_4(\text{NO}_3)_6 \cdot \text{H}_2\text{O}$ (832.2 mAh g^{-1}) and $[\text{Bi}_6\text{O}_4](\text{OH})_4(\text{NO}_3)_6 \cdot \text{H}_2\text{O}/\text{C}$ ($1169.3 \text{ mAh g}^{-1}$). However, the capacity retention (60.3%) and reversible specific capacity (365.5 mAh g^{-1}) of $[\text{Bi}_6\text{O}_4](\text{OH})_4(\text{NO}_3)_6 \cdot \text{H}_2\text{O}/\text{C}$ are much higher than those of $[\text{Bi}_6\text{O}_4](\text{OH})_4(\text{NO}_3)_6 \cdot \text{H}_2\text{O}$ (4.75% and 39.6 mAh g^{-1}) and $[\text{Bi}_6\text{O}_4](\text{OH})_4(\text{NO}_3)_6 \cdot 4\text{H}_2\text{O}$ (15.9% and 289.4 mAh g^{-1}) in the first 30 cycles. The improved electrochemical properties are attributed to the decrease of crystal water in the structure and the introduction of carbon black as conductive additive and volume change buffer. The reaction mechanism of $[\text{Bi}_6\text{O}_4](\text{OH})_4(\text{NO}_3)_6 \cdot \text{H}_2\text{O}/\text{C}$ with Li is also studied in detail by using various *ex-situ* and *in-situ* techniques during the initial charge-discharge cycle. It can be found that the electrochemical reaction of $[\text{Bi}_6\text{O}_4](\text{OH})_4(\text{NO}_3)_6 \cdot \text{H}_2\text{O}$ with Li leads to the preliminary formation of metal Bi, LiNO_3 , LiOH , Li_2O and H_2O and then the alloying reaction to form Li–Bi alloys.

© 2014 Elsevier B.V. All rights reserved.

1. Introduction

With the increasing demands for using portable electronic devices in modern information-rich society, lithium ion batteries have

a large number of commercial applications [1–4]. Many developments in various electronic applications require long cycle life, high energy density and little memory effect. Despite many electrode materials, such as LiCoO_2 , LiMn_2O_4 and LiFePO_4 , have been used in commercial lithium-ion batteries in the past two decades, the reversible conversion reactions of oxides [5,6], nitrides [7,8] and fluorides [9–11] with Li are still intensively studied at the present day. Among various proposed electrode materials, oxides is

* Corresponding author. Tel.: +86 574 87600787; fax: +86 574 87609987.

E-mail addresses: sergio_shu@hotmail.com, shujie@nbu.edu.cn (J. Shu).

one of the most favored electrodes in lithium ion batteries for their higher specific capacity and better rate property than commercial carbonaceous anodes. At the same time, nitrides as a potential electrode candidate with high reversibility also have attracted attentions in recent years.

Recently, bismuth-based compounds as anode materials have been conducted intensive studies [12–16]. For instance, mineral bismuthinite (Bi_2S_3) has been used widely as thermoelectricity and photovoltaic materials. In addition, it expressed good electrochemical properties and chemical behavior with lithium ions. In order to improve cycle performance, $\text{Bi}_2\text{S}_3/\text{C}$ nanocomposite was synthesized and showed a better cycle retention than the pristine sample [15]. The alloying of Bi with Li made the bismuth-based compounds have higher specific capacity than carbonaceous materials [13]. However, the shortcomings of poor cycle performance and the mechanical instability hinder its widely application. Therefore, many developing steps, such as incorporating carbon or nanotubes, are carried out to enhance electrical conductivity and mechanical properties.

Although carbon-based anode materials are widely used and dominate the market of commercial lithium-ion batteries, metal nitrides (such as CoN [17], Sb_3N [18], CrN [19], etc) have been considered as a kind of potential electrode candidates in recent years due to their high reversibility, large reversible capacity and low insertion potentials. However, the nitrides suffered from their obstacles such as large polarization during the charge–discharge cycles. In addition, huge volume changes occurred with the formation of metal-Li alloys, leading to the crushing and pulverization of the electrode. For these reasons, many efforts should be done to explore new electrode materials to suppress polarization, volume change and irreversible capacity loss during the charge and discharge process.

In this paper, $[\text{Bi}_6\text{O}_4](\text{OH})_4(\text{NO}_3)_6 \cdot 4\text{H}_2\text{O}$ and $[\text{Bi}_6\text{O}_4](\text{OH})_4(\text{NO}_3)_6 \cdot \text{H}_2\text{O}$ are firstly investigated as novel anode materials for lithium ion batteries. Furthermore, $[\text{Bi}_6\text{O}_4](\text{OH})_4(\text{NO}_3)_6 \cdot \text{H}_2\text{O}/\text{C}$ composite is also synthesized and its electrochemical performance is carefully studied by charge–discharge cycle and cyclic voltammogram (CV). Besides, probable lithium insertion and extraction mechanisms during discharge and charge process are proposed according to the *ex-situ* Fourier transform infrared spectrometry (FTIR), *ex-situ* high resolution transmission electron microscopy (HRTEM), selected area electron diffraction (SAED) images, *ex-situ* X-ray diffraction (XRD) and *in-situ* XRD analysis.

2. Experimental

In this experiment, $\text{Bi}(\text{NO}_3)_3 \cdot 5\text{H}_2\text{O}$ was of analytical grade and purchased from Guanghai Chemical Reagent Shantou Co. Ltd in China. $\text{Bi}(\text{NO}_3)_3 \cdot 5\text{H}_2\text{O}/\text{C}$ composite was synthesized by mixing of $\text{Bi}(\text{NO}_3)_3 \cdot 5\text{H}_2\text{O}$ (1.0 g) and carbon black (200 mg) in ethyl alcohol under continuous stirring for 10 h. The solvent was evaporated at 60 °C and the resulting black powder is $\text{Bi}(\text{NO}_3)_3 \cdot 5\text{H}_2\text{O}/\text{C}$. Then, $\text{Bi}(\text{NO}_3)_3 \cdot 5\text{H}_2\text{O}/\text{C}$ was heat-treated at 120 °C in a vacuum oven for 24 h to fabricate the objective sample, which can be preliminarily defined as $\text{Bi}(\text{NO}_3)_3 \cdot 5\text{H}_2\text{O}/\text{C}-120$. For comparison, carbon free bismuth nitrates were synthesized by two routes. Sample A was obtained by direct heating $\text{Bi}(\text{NO}_3)_3 \cdot 5\text{H}_2\text{O}$ at 120 °C in a vacuum oven for 24 h, which was preliminarily defined as $\text{Bi}(\text{NO}_3)_3 \cdot 5\text{H}_2\text{O}-120\text{A}$. Sample B was prepared by dissolving $\text{Bi}(\text{NO}_3)_3 \cdot 5\text{H}_2\text{O}$ in ethyl alcohol under continuous stirring for 10 h. The solvent was evaporated at 60 °C and the resulting powder was put in vacuum oven at 120 °C for 24 h to form the objective sample, which was preliminarily defined as $\text{Bi}(\text{NO}_3)_3 \cdot 5\text{H}_2\text{O}-120\text{B}$.

To fabricate working electrode, a homogeneous slurry was formed by using $\text{Bi}(\text{NO}_3)_3 \cdot 5\text{H}_2\text{O}-120\text{A}$ or $\text{Bi}(\text{NO}_3)_3 \cdot 5\text{H}_2\text{O}-120\text{B}$ as

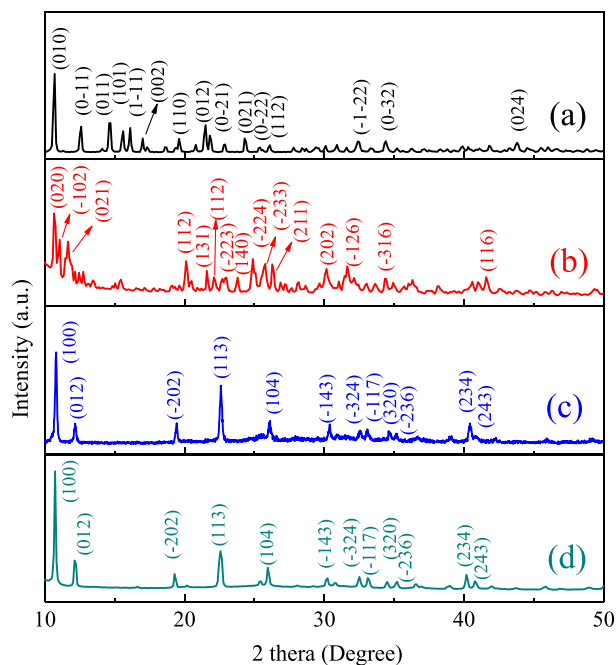


Fig. 1. XRD patterns of as-obtained samples. (a) The pristine $\text{Bi}(\text{NO}_3)_3 \cdot 5\text{H}_2\text{O}$; (b) $[\text{Bi}_6\text{O}_4](\text{OH})_4(\text{NO}_3)_6 \cdot 4\text{H}_2\text{O}$; (c) $[\text{Bi}_6\text{O}_4](\text{OH})_4(\text{NO}_3)_6 \cdot \text{H}_2\text{O}$; and (d) $[\text{Bi}_6\text{O}_4](\text{OH})_4(\text{NO}_3)_6 \cdot \text{H}_2\text{O}/\text{C}$.

active material (70 wt.%), carbon black as conductive additive (20 wt.%) and polyvinylidene fluoride as binder (10 wt.%) in N-methylpyrrolidinone. For $\text{Bi}(\text{NO}_3)_3 \cdot 5\text{H}_2\text{O}/\text{C}-120$, the homogeneous slurry was formed by using $\text{Bi}(\text{NO}_3)_3 \cdot 5\text{H}_2\text{O}/\text{C}-120$ as active material (84 wt.%), carbon black as conductive additive (6 wt.%) and polyvinylidene fluoride as binder (10 wt.%) in N-methylpyrrolidinone. Next, the slurry was uniformly spread on Cu foil by a doctor-blade technique and this as-obtained film was dried at 120 °C in a vacuum oven for 24 h. Then a lot of discs were cut with a diameter of 15 mm and used as the working electrodes for investigation.

The simulated half cells, using the fabricated electrode as cathode, lithium disc as anode and Whaman glass fiber as separator, were assembled in an argon-filled glove box. The Li-containing electrolyte is 1 mol L^{-1} LiPF_6 solution with the solvent composition of ethylene carbonate and dimethyl carbonate by a volume proportion of 1:1. The charge–discharge tests were conducted on a multi-channel Land battery test system (Wuhan Jinnuo, China) at a constant current of 50 mA g^{-1} between 0.0 and 3.4 V

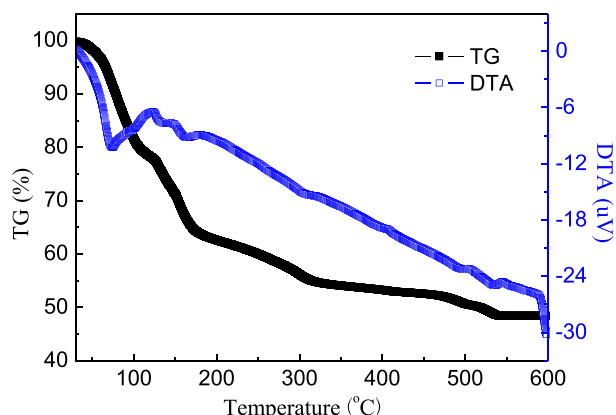


Fig. 2. TG–DTA curves of $\text{Bi}(\text{NO}_3)_3 \cdot 5\text{H}_2\text{O}$ in argon.

and the cyclic voltammograms were measured on CHI 1000B electrochemical workstation (Shanghai Chenhua, China) at a scan rate of 0.1 mV s^{-1} between 0.0 and 3.4 V at room temperature. Electrochemical impedance spectra of as-prepared electrodes were collected by a CHI 660D electrochemical workstation (Shanghai Chenhua, China) with the frequency range between 100000 and 0.01 Hz.

Thermogravimetric (TG) and differential thermal analysis (DTA) behaviors of $\text{Bi}(\text{NO}_3)_3 \cdot 5\text{H}_2\text{O}$ were obtained by a Seiko TG/DTA 6300 instrument under argon atmosphere. The structural evolutions of the samples were measured by Bruker AXS D8 Focus X-ray diffraction instrument with $\text{Cu K}\alpha$ radiation. Samples were observed with a scan angle range from 10 to 80° , a step size of 0.1° and a count time of 1 s. The powder morphology was observed

using a field emission scanning electron microscopy (FE-SEM, LEO 1530). Moreover, structural evolutions of active material during charge-discharge cycles were observed by using a Shimadzu FTIR-8900 Fourier transform infrared spectrometry between 500 and 2500 cm^{-1} . *Ex-situ* HRTEM and corresponding SAED images were observed by using JEOL JEM-2100 high resolution transmission electron microscopy.

3. Result and discussion

Phase purity of as-obtained materials was obtained using X-ray diffraction technique. Fig. 1 shows the XRD patterns of pristine $\text{Bi}(\text{NO}_3)_3 \cdot 5\text{H}_2\text{O}$ and as-prepared active materials. Fig. 1a shows the XRD pattern of pristine $\text{Bi}(\text{NO}_3)_3 \cdot 5\text{H}_2\text{O}$ powder (JCPDS card No.12-

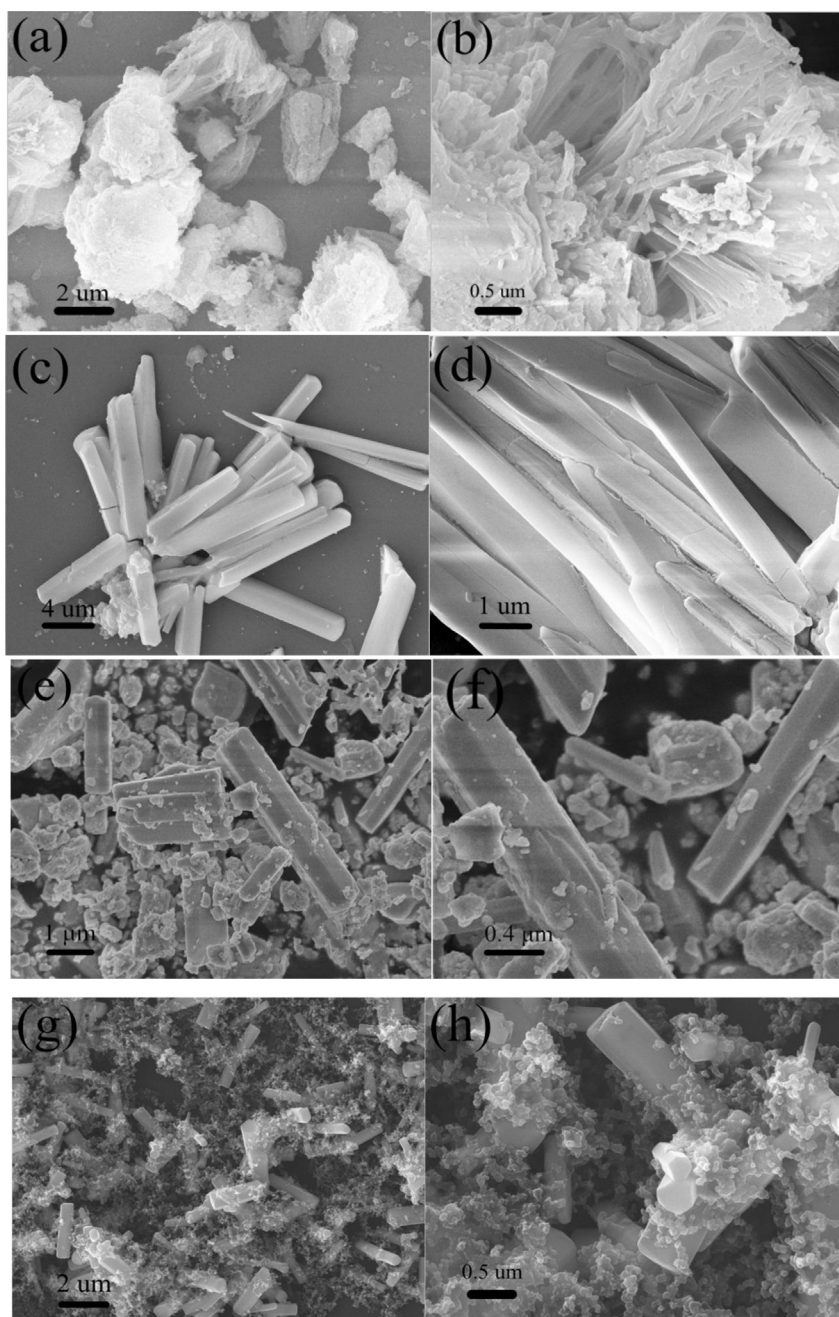


Fig. 3. SEM images of as-obtained samples. (a, b) The pristine $\text{Bi}(\text{NO}_3)_3 \cdot 5\text{H}_2\text{O}$; (c, d) $[\text{Bi}_6\text{O}_4](\text{OH})_4(\text{NO}_3)_6 \cdot 4\text{H}_2\text{O}$; (e, f) $[\text{Bi}_6\text{O}_4](\text{OH})_4(\text{NO}_3)_6 \cdot \text{H}_2\text{O}$; (g, h) $[\text{Bi}_6\text{O}_4](\text{OH})_4(\text{NO}_3)_6 \cdot \text{H}_2\text{O}/\text{C}$.

0148), which is a kind of anorthic crystal structure and its space group is P-1 (No. 2) and its cell parameter is $a = 6.520 \text{ \AA}$, $b = 8.642 \text{ \AA}$, $c = 10.683 \text{ \AA}$, $\alpha = 100.82^\circ$, $\beta = 80.78^\circ$ and $\gamma = 104.77^\circ$. After a direct heat-treatment under vacuum, the XRD pattern of $\text{Bi}(\text{NO}_3)_3 \cdot 5\text{H}_2\text{O}$ -120A in Fig. 1b can be indexed to the characteristic structure of $[\text{Bi}_6\text{O}_4](\text{OH})_4(\text{NO}_3)_6 \cdot 4\text{H}_2\text{O}$ (JCPDS card No. 84-2189) that belongs to monoclinic crystal structure and its space group is $P2_1/c$ (No. 14) and the cell parameters are $a = 9.059 \text{ \AA}$, $b = 17.05 \text{ \AA}$, $c = 18.269 \text{ \AA}$ and $\beta = 120.00^\circ$. Fig. 1c and d show the featured XRD patterns of $\text{Bi}(\text{NO}_3)_3 \cdot 5\text{H}_2\text{O}$ -120B and $\text{Bi}(\text{NO}_3)_3 \cdot 5\text{H}_2\text{O}/\text{C}$ -120, respectively. Based on the JCPDS card No. 71-1360, the two samples reveals the same crystal structure and space group as that of $[\text{Bi}_6\text{O}_4](\text{OH})_4(\text{NO}_3)_6 \cdot \text{H}_2\text{O}$. Their cell parameters are $a = 9.289 \text{ \AA}$, $b = 13.46 \text{ \AA}$, $c = 19.527 \text{ \AA}$ and $\beta = 114.13^\circ$.

Fig. 2 shows the TG-DTA curves of $\text{Bi}(\text{NO}_3)_3 \cdot 5\text{H}_2\text{O}$ powder under argon atmosphere. There are four steps, 20–120 °C, 120–180 °C, 180–320 °C and 320–550 °C, appeared in the TG curve during weight loss process. The first weight loss of 21.8% between 20 and 120 °C can be attributed to the partial loss of crystal water and NO_3 in $\text{Bi}(\text{NO}_3)_3 \cdot 5\text{H}_2\text{O}$ to form $[\text{Bi}_6\text{O}_4](\text{OH})_4(\text{NO}_3)_6 \cdot 4\text{H}_2\text{O}$. It indicates that $\text{Bi}(\text{NO}_3)_3 \cdot 5\text{H}_2\text{O}$ transforms into $[\text{Bi}_6\text{O}_4](\text{OH})_4(\text{NO}_3)_6 \cdot 4\text{H}_2\text{O}$ after a direct heat-treatment under vacuum. Other three weight losses in the TG curves can be contributed to the decomposition of $[\text{Bi}_6\text{O}_4](\text{OH})_4(\text{NO}_3)_6 \cdot 4\text{H}_2\text{O}$ and the final formation of Bi_2O_3 . Combined with XRD result, the weight loss in TG curve indicates that $[\text{Bi}_6\text{O}_4](\text{OH})_4(\text{NO}_3)_6 \cdot \text{H}_2\text{O}$ cannot be obtained by a direct heat-treatment under vacuum but formed after recrystallization in ethyl alcohol and dehydration. As a result, the as-prepared $\text{Bi}(\text{NO}_3)_3 \cdot 5\text{H}_2\text{O}$ -120A, $\text{Bi}(\text{NO}_3)_3 \cdot 5\text{H}_2\text{O}$ -120B and $\text{Bi}(\text{NO}_3)_3 \cdot 5\text{H}_2\text{O}/\text{C}$ -120 can respectively be described as $[\text{Bi}_6\text{O}_4](\text{OH})_4(\text{NO}_3)_6 \cdot 4\text{H}_2\text{O}$, $[\text{Bi}_6\text{O}_4](\text{OH})_4(\text{NO}_3)_6 \cdot \text{H}_2\text{O}$ and $[\text{Bi}_6\text{O}_4](\text{OH})_4(\text{NO}_3)_6 \cdot \text{H}_2\text{O}/\text{C}$ in the following section.

The SEM images reveal the morphologies of the pristine $\text{Bi}(\text{NO}_3)_3 \cdot 5\text{H}_2\text{O}$, $[\text{Bi}_6\text{O}_4](\text{OH})_4(\text{NO}_3)_6 \cdot 4\text{H}_2\text{O}$, $[\text{Bi}_6\text{O}_4](\text{OH})_4(\text{NO}_3)_6 \cdot \text{H}_2\text{O}$

and $[\text{Bi}_6\text{O}_4](\text{OH})_4(\text{NO}_3)_6 \cdot \text{H}_2\text{O}/\text{C}$ as shown in Fig. 3. Fig. 3a and b show the surface morphology of the pristine $\text{Bi}(\text{NO}_3)_3 \cdot 5\text{H}_2\text{O}$. It can be clearly observed that the original $\text{Bi}(\text{NO}_3)_3 \cdot 5\text{H}_2\text{O}$ is composed of blocks about $2 \mu\text{m}$ in diameter. Furthermore, the blocks consist of clusters of nanowires with 100 nm in diameter as shown in Fig. 3b. For comparison, the morphology of $[\text{Bi}_6\text{O}_4](\text{OH})_4(\text{NO}_3)_6 \cdot 4\text{H}_2\text{O}$ changes obviously after the pristine $\text{Bi}(\text{NO}_3)_3 \cdot 5\text{H}_2\text{O}$ heat-treatment at 120°C as shown in Fig. 3c and d. It exhibits the clusters of rods with $2 \mu\text{m}$ in diameter and $6\text{--}8 \mu\text{m}$ in length. After recrystallization, the surface morphology of $[\text{Bi}_6\text{O}_4](\text{OH})_4(\text{NO}_3)_6 \cdot \text{H}_2\text{O}$ powder can be observed in Fig. 3e and f. It shows similar rod-like shape with that of $[\text{Bi}_6\text{O}_4](\text{OH})_4(\text{NO}_3)_6 \cdot 4\text{H}_2\text{O}$ but displays smaller size (about $0.5 \mu\text{m}$ in diameter and $3\text{--}4 \mu\text{m}$ in length). After coating by carbon black, the surface morphology of $[\text{Bi}_6\text{O}_4](\text{OH})_4(\text{NO}_3)_6 \cdot \text{H}_2\text{O}/\text{C}$ is shown in Fig. 3g and h. It shows similar rod-like shape with that of $[\text{Bi}_6\text{O}_4](\text{OH})_4(\text{NO}_3)_6 \cdot \text{H}_2\text{O}$. Moreover, these rods are well dispersed in carbon black matrix providing larger area for Li^+ ions diffusion and higher electronic conductivity. It indicates that the $[\text{Bi}_6\text{O}_4](\text{OH})_4(\text{NO}_3)_6 \cdot \text{H}_2\text{O}/\text{C}$ composite will exhibit a better cycle performance.

Fig. 4a–c illustrates the first three cyclic voltammograms for the as-obtained film electrodes of $[\text{Bi}_6\text{O}_4](\text{OH})_4(\text{NO}_3)_6 \cdot 4\text{H}_2\text{O}$, $[\text{Bi}_6\text{O}_4](\text{OH})_4(\text{NO}_3)_6 \cdot \text{H}_2\text{O}$ and $[\text{Bi}_6\text{O}_4](\text{OH})_4(\text{NO}_3)_6 \cdot \text{H}_2\text{O}/\text{C}$ between 0.0 and 3.4 V with a scan rate of 0.1 mV s^{-1} . There are three reduction peaks at about 1.67, 1.42 and 0.40 V and five oxidation peaks at around 1.02, 1.32, 1.80, 2.54 and 2.84 V in the initial cycle of $[\text{Bi}_6\text{O}_4](\text{OH})_4(\text{NO}_3)_6 \cdot 4\text{H}_2\text{O}$ as shown in Fig. 4a. During the subsequent scan, four reduction peaks at 1.53, 1.33, 0.47, 0.12 V and five oxidation peaks at 0.99, 1.33, 1.79, 2.47, 2.97 V can be observed. It suggests that the electrochemical reaction of $[\text{Bi}_6\text{O}_4](\text{OH})_4(\text{NO}_3)_6 \cdot 4\text{H}_2\text{O}$ with Li is a complex process. After recrystallization in ethyl alcohol, four reduction peaks at 2.28, 1.35, 1.11, 0.32 V and three oxidation peaks at 1.08, 2.36, 2.95 V can be observed for $[\text{Bi}_6\text{O}_4](\text{OH})_4(\text{NO}_3)_6 \cdot \text{H}_2\text{O}$ as shown in Fig. 4b. In contrast, six reduction peaks at 2.26, 1.46, 0.97 ,

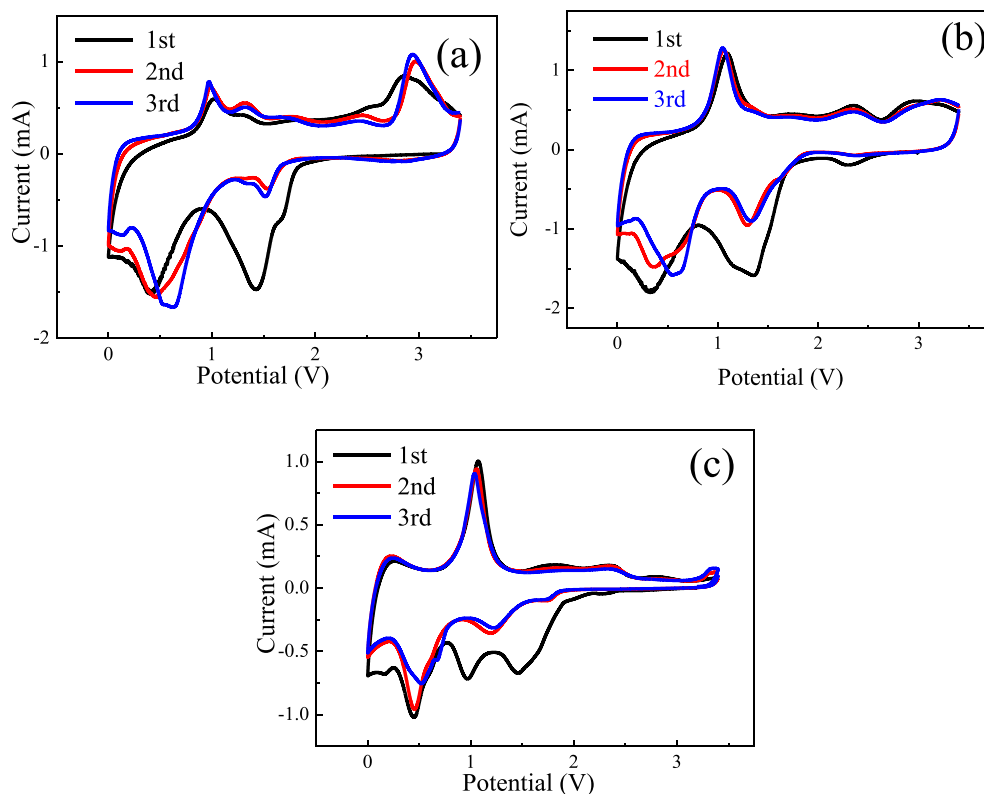


Fig. 4. Cyclic voltammogram curves of (a) $[\text{Bi}_6\text{O}_4](\text{OH})_4(\text{NO}_3)_6 \cdot 4\text{H}_2\text{O}$, (b) $[\text{Bi}_6\text{O}_4](\text{OH})_4(\text{NO}_3)_6 \cdot \text{H}_2\text{O}$ and (c) $[\text{Bi}_6\text{O}_4](\text{OH})_4(\text{NO}_3)_6 \cdot \text{H}_2\text{O}/\text{C}$.

0.60, 0.45, 0.16 V and five oxidation peaks at 0.23, 1.07, 1.84, 2.39, 2.82 V appear in the initial cycle of $[\text{Bi}_6\text{O}_4](\text{OH})_4(\text{NO}_3)_6 \cdot \text{H}_2\text{O}/\text{C}$ as shown in Fig. 4c. The evolution of redox peaks should be attributed to the partial loss of crystal water, carbon coating and the change of surface morphology and particle size. Besides, the irreversible reduction peak at 1.0 V should be contributed to the irreversible electrolyte decomposition reaction on carbon black (Supplementary materials). In the second scan, $[\text{Bi}_6\text{O}_4](\text{OH})_4(\text{NO}_3)_6 \cdot \text{H}_2\text{O}$ and $[\text{Bi}_6\text{O}_4](\text{OH})_4(\text{NO}_3)_6 \cdot \text{H}_2\text{O}/\text{C}$ show similar redox peaks as shown in Fig. 4b and c. For $[\text{Bi}_6\text{O}_4](\text{OH})_4(\text{NO}_3)_6 \cdot \text{H}_2\text{O}/\text{C}$, it reveals four reduction peaks at 1.73, 1.20, 0.62, 0.46 V and five oxidation peaks at 0.23, 1.05, 1.88, 2.34, 2.84 V in the second cycle. It can also be found that most redox peaks of $[\text{Bi}_6\text{O}_4](\text{OH})_4(\text{NO}_3)_6 \cdot \text{H}_2\text{O}$ and $[\text{Bi}_6\text{O}_4](\text{OH})_4(\text{NO}_3)_6 \cdot \text{H}_2\text{O}/\text{C}$ appear at similar potentials with those of $[\text{Bi}_6\text{O}_4](\text{OH})_4(\text{NO}_3)_6 \cdot 4\text{H}_2\text{O}$ electrode. The difference in the peak current at 0.23 and 0.97 V suggests that the introduction of carbon black changes the lithium storage behaviors in Li-alloying reaction at low potential region, which is familiar with the results of other Bi-based composites as anode materials for lithium-ion batteries [12–14]. Moreover, some additional charge capacity also comes from the lithium storage in carbon (Supplementary materials), which results in the higher oxidation peak at 0.97 V for $[\text{Bi}_6\text{O}_4](\text{OH})_4(\text{NO}_3)_6 \cdot \text{H}_2\text{O}/\text{C}$ than that of $[\text{Bi}_6\text{O}_4](\text{OH})_4(\text{NO}_3)_6 \cdot 4\text{H}_2\text{O}$ and $[\text{Bi}_6\text{O}_4](\text{OH})_4(\text{NO}_3)_6 \cdot \text{H}_2\text{O}$. As reported [20,21], the redox polarization of electrochemical process and the formation/decomposition of SEI film can be greatly affected by the water content in electrolyte. During the irreversible decomposition process, different water amount was produced by $[\text{Bi}_6\text{O}_4](\text{OH})_4(\text{NO}_3)_6 \cdot 4\text{H}_2\text{O}$ and $[\text{Bi}_6\text{O}_4](\text{OH})_4(\text{NO}_3)_6 \cdot \text{H}_2\text{O}/\text{C}$ (or $[\text{Bi}_6\text{O}_4](\text{OH})_4(\text{NO}_3)_6 \cdot \text{H}_2\text{O}$). As a result, the existence of different water

content in electrolyte results in the slight difference of some redox peaks for $[\text{Bi}_6\text{O}_4](\text{OH})_4(\text{NO}_3)_6 \cdot 4\text{H}_2\text{O}$ and $[\text{Bi}_6\text{O}_4](\text{OH})_4(\text{NO}_3)_6 \cdot \text{H}_2\text{O}/\text{C}$ (or $[\text{Bi}_6\text{O}_4](\text{OH})_4(\text{NO}_3)_6 \cdot \text{H}_2\text{O}$) in CV curves. Besides, much more water in electrolyte of $[\text{Bi}_6\text{O}_4](\text{OH})_4(\text{NO}_3)_6 \cdot 4\text{H}_2\text{O}$ battery also induces the more noticeable electrochemical decomposition of SEI film above 2.5 V.

Fig. 5a–c shows the charge–discharge curves of $[\text{Bi}_6\text{O}_4](\text{OH})_4(\text{NO}_3)_6 \cdot 4\text{H}_2\text{O}$, $[\text{Bi}_6\text{O}_4](\text{OH})_4(\text{NO}_3)_6 \cdot \text{H}_2\text{O}$ and $[\text{Bi}_6\text{O}_4](\text{OH})_4(\text{NO}_3)_6 \cdot \text{H}_2\text{O}/\text{C}$ as anode materials in the first three cycles at a current density of 50 mA g^{-1} . The first discharge specific capacities for $[\text{Bi}_6\text{O}_4](\text{OH})_4(\text{NO}_3)_6 \cdot 4\text{H}_2\text{O}$, $[\text{Bi}_6\text{O}_4](\text{OH})_4(\text{NO}_3)_6 \cdot \text{H}_2\text{O}$ and $[\text{Bi}_6\text{O}_4](\text{OH})_4(\text{NO}_3)_6 \cdot \text{H}_2\text{O}/\text{C}$ between 0.0 and 3.4 V are 2792.9, 1376.5 and 1169.3 mAh g^{-1} , and the corresponding initial columbic efficiencies are 65.1, 60.5 and 51.9%, respectively. It indicates that the irreversible formation of solid electrolyte interphase (SEI) film and structural breakdown take place during the first discharge process. For $[\text{Bi}_6\text{O}_4](\text{OH})_4(\text{NO}_3)_6 \cdot 4\text{H}_2\text{O}$, the initial lithiation plateaus at around 1.65, 0.78 and 0.14 V in Fig. 5a correspond to the electrochemical decomposition of $[\text{Bi}_6\text{O}_4](\text{OH})_4(\text{NO}_3)_6 \cdot 4\text{H}_2\text{O}$ and the formation of Li–Bi alloys [13,15]. After recrystallization and carbon coating, $[\text{Bi}_6\text{O}_4](\text{OH})_4(\text{NO}_3)_6 \cdot \text{H}_2\text{O}$ and $[\text{Bi}_6\text{O}_4](\text{OH})_4(\text{NO}_3)_6 \cdot \text{H}_2\text{O}/\text{C}$ shows similar lithiation–delithiation plateaus as shown in Fig. 5b and c, respectively. For $[\text{Bi}_6\text{O}_4](\text{OH})_4(\text{NO}_3)_6 \cdot \text{H}_2\text{O}/\text{C}$, these lithiation plateaus appear at the potentials of 1.19, 0.63 and 0.13 V in the first discharge process, which are close to the reduction peaks of cyclic voltammograms as shown in Fig. 4c. Besides, a longer slope appears at 1.65 V for $[\text{Bi}_6\text{O}_4](\text{OH})_4(\text{NO}_3)_6 \cdot \text{H}_2\text{O}$ and $[\text{Bi}_6\text{O}_4](\text{OH})_4(\text{NO}_3)_6 \cdot \text{H}_2\text{O}/\text{C}$ than that of $[\text{Bi}_6\text{O}_4](\text{OH})_4(\text{NO}_3)_6 \cdot 4\text{H}_2\text{O}$, which suggests that the electrochemical behaviors of $[\text{Bi}_6\text{O}_4](\text{OH})_4(\text{NO}_3)_6 \cdot 4\text{H}_2\text{O}$ are changed by recrystallization and carbon coating. Upon delithiation,

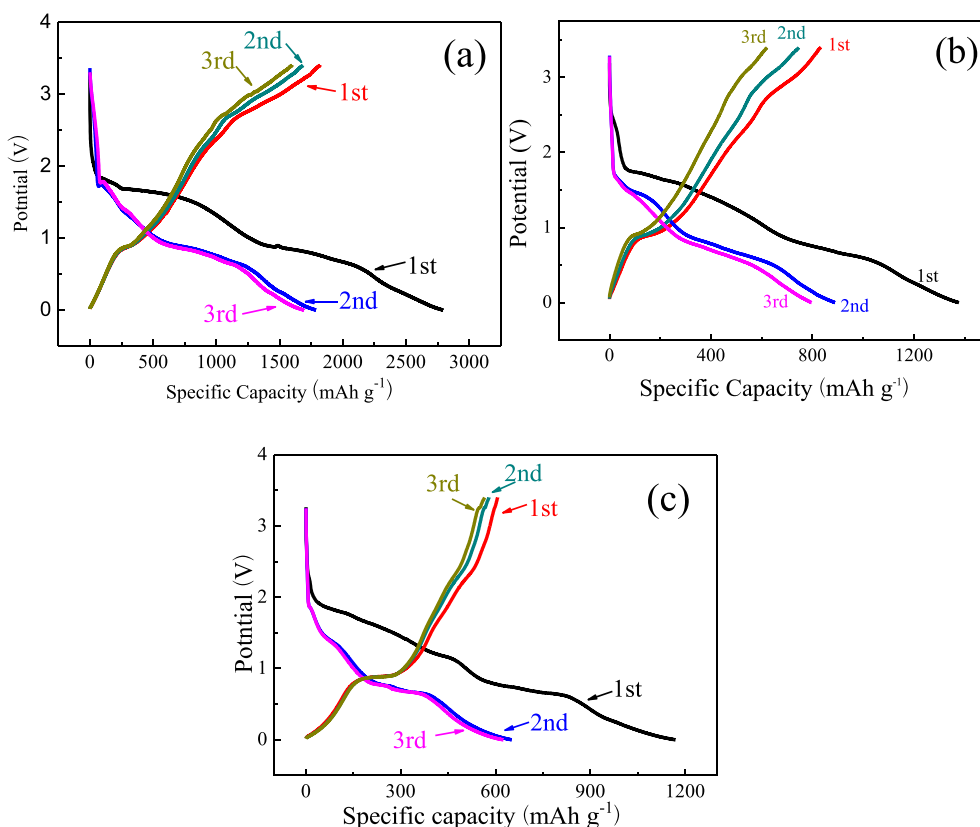


Fig. 5. Charge–discharge curves of (a) $[\text{Bi}_6\text{O}_4](\text{OH})_4(\text{NO}_3)_6 \cdot 4\text{H}_2\text{O}$, (b) $[\text{Bi}_6\text{O}_4](\text{OH})_4(\text{NO}_3)_6 \cdot \text{H}_2\text{O}$ and (c) $[\text{Bi}_6\text{O}_4](\text{OH})_4(\text{NO}_3)_6 \cdot \text{H}_2\text{O}/\text{C}$ between 0.0 and 3.4 V at a current density of 50 mA g^{-1} .

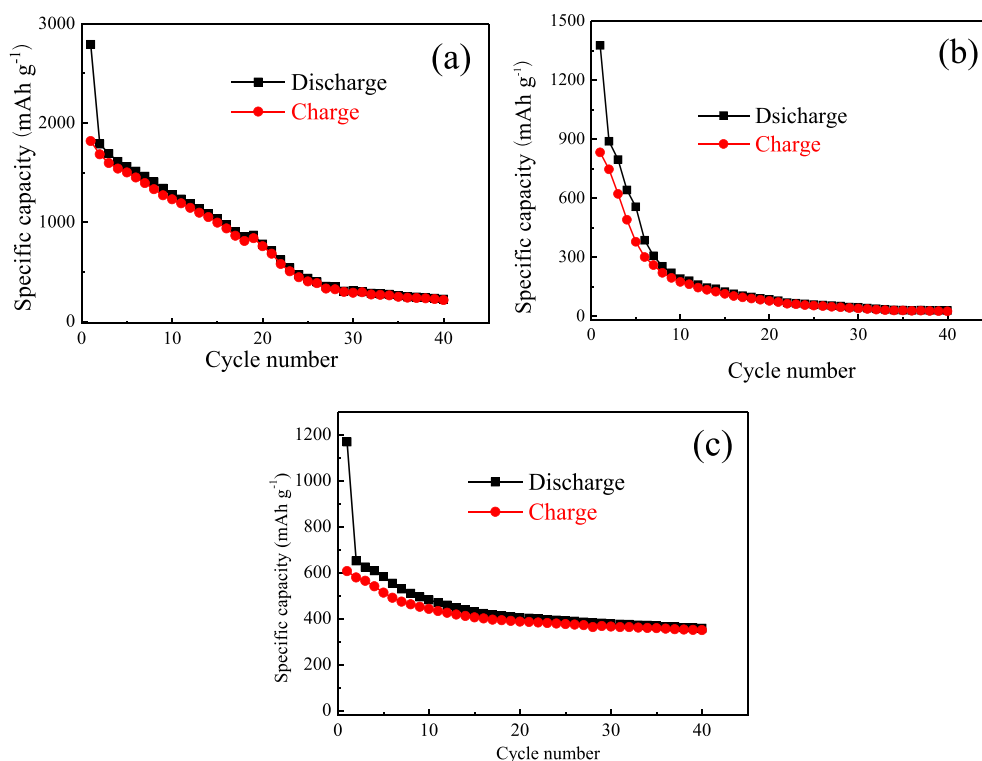


Fig. 6. Cycling properties of (a) $[\text{Bi}_6\text{O}_4](\text{OH})_4(\text{NO}_3)_6 \cdot 4\text{H}_2\text{O}$, (b) $[\text{Bi}_6\text{O}_4](\text{OH})_4(\text{NO}_3)_6 \cdot \text{H}_2\text{O}$ and (c) $[\text{Bi}_6\text{O}_4](\text{OH})_4(\text{NO}_3)_6 \cdot \text{H}_2\text{O}/\text{C}$.

$[\text{Bi}_6\text{O}_4](\text{OH})_4(\text{NO}_3)_6 \cdot 4\text{H}_2\text{O}$ shows one plateau at 0.87 V and one slope at 3.00 V. The capacity in this high potential slope may come from side reactions, such as the decomposition of SEI film. In contrast, the long slope at 3.0 V disappears after carbon coating as shown in Fig. 5c. It suggests that $[\text{Bi}_6\text{O}_4](\text{OH})_4(\text{NO}_3)_6 \cdot \text{H}_2\text{O}/\text{C}$ can be used as high capacity anode material with long-term cycleability.

To compare the cycle performance of $[\text{Bi}_6\text{O}_4](\text{OH})_4(\text{NO}_3)_6 \cdot 4\text{H}_2\text{O}$, $[\text{Bi}_6\text{O}_4](\text{OH})_4(\text{NO}_3)_6 \cdot \text{H}_2\text{O}$ and $[\text{Bi}_6\text{O}_4](\text{OH})_4(\text{NO}_3)_6 \cdot \text{H}_2\text{O}/\text{C}$, the specific capacity as a function of cycle number of three electrodes is intuitively shown in Fig. 6a, b and c, respectively. It is clear that $[\text{Bi}_6\text{O}_4](\text{OH})_4(\text{NO}_3)_6 \cdot 4\text{H}_2\text{O}$ electrode shows higher initial charge capacity ($1818.6 \text{ mAh g}^{-1}$) and reversible specific capacity (403.1 mAh g^{-1}) than those of $[\text{Bi}_6\text{O}_4](\text{OH})_4(\text{NO}_3)_6 \cdot \text{H}_2\text{O}$ (832.2 and 54.4 mAh g^{-1}) and $[\text{Bi}_6\text{O}_4](\text{OH})_4(\text{NO}_3)_6 \cdot \text{H}_2\text{O}/\text{C}$ (606.6 and 376.3 mAh g^{-1}) in the first 25 cycles. However, $[\text{Bi}_6\text{O}_4](\text{OH})_4(\text{NO}_3)_6 \cdot \text{H}_2\text{O}/\text{C}$ composite exhibits better cycle performance than that of $[\text{Bi}_6\text{O}_4](\text{OH})_4(\text{NO}_3)_6 \cdot \text{H}_2\text{O}$ and $[\text{Bi}_6\text{O}_4](\text{OH})_4(\text{NO}_3)_6 \cdot 4\text{H}_2\text{O}$. The capacity retention (60.3%) and reversible specific capacity (365.5 mAh g^{-1}) of $[\text{Bi}_6\text{O}_4](\text{OH})_4(\text{NO}_3)_6 \cdot \text{H}_2\text{O}/\text{C}$ are much higher than those of bare $[\text{Bi}_6\text{O}_4](\text{OH})_4(\text{NO}_3)_6 \cdot \text{H}_2\text{O}$ (4.75% and 39.6 mAh g^{-1}) and $[\text{Bi}_6\text{O}_4](\text{OH})_4(\text{NO}_3)_6 \cdot 4\text{H}_2\text{O}$ (15.9% and 289.4 mAh g^{-1}) in the first 30 cycles. It is clear that the charge specific capacity of $[\text{Bi}_6\text{O}_4](\text{OH})_4(\text{NO}_3)_6 \cdot 4\text{H}_2\text{O}$ decreases sharply upon repeated cycles. The capacity loss per cycle is 2.1% in the first 40 cycles, which is much higher than the value (0.99%) of $[\text{Bi}_6\text{O}_4](\text{OH})_4(\text{NO}_3)_6 \cdot \text{H}_2\text{O}/\text{C}$ composite. It can be concluded that $[\text{Bi}_6\text{O}_4](\text{OH})_4(\text{NO}_3)_6 \cdot \text{H}_2\text{O}/\text{C}$ composite obtains a better cyclic performance due to the introduction of conductive carbon buffer to maintain the electrode stability and improve the electronic conductivity as the EIS patterns shown in Fig. 7. Here, all the EIS spectra of $[\text{Bi}_6\text{O}_4](\text{OH})_4(\text{NO}_3)_6 \cdot 4\text{H}_2\text{O}$ and $[\text{Bi}_6\text{O}_4](\text{OH})_4(\text{NO}_3)_6 \cdot \text{H}_2\text{O}/\text{C}$ are simulated and calculated by using the equivalent circuit as inserted in Fig. 7, and the as-obtained parameters are shown in Table 1. In

the equivalent circuit, R_s is solution and contact resistance, R_{ct} is charge transfer resistance, CPE is constant phase element, and W is Warburg diffusion impedance. As shown in Table 1, it is clear that the R_s (5.036Ω) of $[\text{Bi}_6\text{O}_4](\text{OH})_4(\text{NO}_3)_6 \cdot \text{H}_2\text{O}/\text{C}$ is much lower than that (22.46Ω) of $[\text{Bi}_6\text{O}_4](\text{OH})_4(\text{NO}_3)_6 \cdot 4\text{H}_2\text{O}$. It indicates that the electronic conductivity is greatly improved. Besides, R_{ct} determines the kinetic properties of samples. By a parallel comparison with the calculated data, it is clear that the R_{ct} (15.59Ω) $[\text{Bi}_6\text{O}_4](\text{OH})_4(\text{NO}_3)_6 \cdot \text{H}_2\text{O}/\text{C}$ is also much lower than that (26.20Ω) of $[\text{Bi}_6\text{O}_4](\text{OH})_4(\text{NO}_3)_6 \cdot 4\text{H}_2\text{O}$. Therefore, $[\text{Bi}_6\text{O}_4](\text{OH})_4(\text{NO}_3)_6 \cdot \text{H}_2\text{O}/\text{C}$

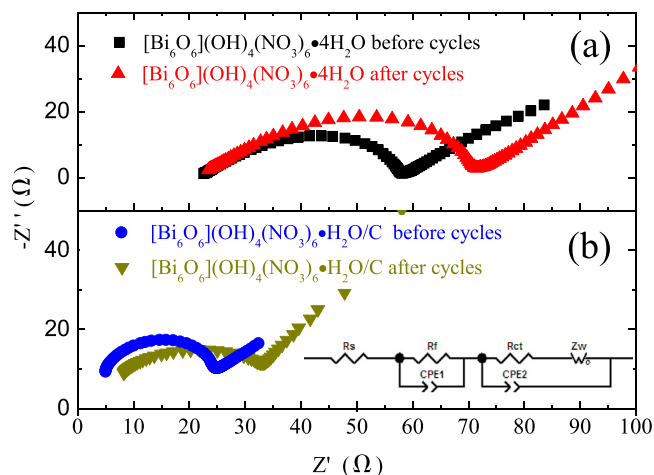


Fig. 7. Electrochemical impedance spectra of (a) $[\text{Bi}_6\text{O}_4](\text{OH})_4(\text{NO}_3)_6 \cdot 4\text{H}_2\text{O}$ and (b) $[\text{Bi}_6\text{O}_4](\text{OH})_4(\text{NO}_3)_6 \cdot \text{H}_2\text{O}/\text{C}$ in a frequency range of 10^5 – 10^{-2} Hz .

Table 1

The simulated data calculated from EIS spectra using the equivalent circuit.

Sample	R_s (Ω)	R_f (Ω)	CPE ₁ (μ F)	R_{ct} (Ω)	CPE ₂ (μ F)	W (Ω)
[Bi ₆ O ₄](OH) ₄ (NO ₃) ₆ ·4H ₂ O before cycles	22.46	0	0	26.20	0.004786	0.09559
[Bi ₆ O ₄](OH) ₄ (NO ₃) ₆ ·4H ₂ O after cycles	23.16	21.21	1.398E-5	35.25	2.277E-5	0.1324
[Bi ₆ O ₄](OH) ₄ (NO ₃) ₆ ·H ₂ O/C before cycles	5.036	0	0	15.59	3.192E-5	0.003985
[Bi ₆ O ₄](OH) ₄ (NO ₃) ₆ ·H ₂ O/C after cycles	10.73	12.65	1.683E-5	19.66	2.79E-5	0.03446

displays better electrochemical properties as lithium storage material.

To investigate the structural transformation of [Bi₆O₄](OH)₄(NO₃)₆·H₂O/C composite, *ex-situ* FTIR and *ex-situ* XRD patterns were collected on the [Bi₆O₄](OH)₄(NO₃)₆·H₂O/C electrodes at selected specific capacity during the initial charge–discharge process. There are five simulated cells dismantled in Ar-filled glove box, which are named as patterns (a)–(e), including patterns (a)–(c) in the first discharge process and patterns (c)–(e) in the initial charge process as shown in Fig. 8a. For the *ex-situ* FTIR analysis, the lithiated and delithiated samples were rinsed by dimethyl carbonate to remove the electrolyte in Ar-filled glove box. The as-prepared samples were dried under vacuum condition for 12 h to remove dimethyl carbonate and then mixed with KBr to form semi-transparent slices for FTIR observation. For comparison, the electrodes for *ex-situ* XRD investigation were directly tested without any further treatment.

Fig. 8b shows the *ex-situ* FTIR analysis ranging from 1100 to 1800 cm^{−1}. The characteristic vibration of NO₃[−] in [Bi₆O₄](OH)₄(NO₃)₆·H₂O/C can be contributed to the band approximately at 1385 cm^{−1} [22]. It can be found that the intensity of characteristic infrared peak for NO₃[−] shows a gradual and slight decrease during the electrochemical lithiation process as shown in Fig. 8b. However, the characteristic peak of NO₃[−] does not disappear at the end of discharge process, which indicates an irreversible phase transformation reaction from [Bi₆O₄](OH)₄(NO₃)₆·H₂O/C to LiNO₃. Besides, Fig. 8b shows that the intensity of characteristic peak for NO₃[−] has no evolution during the delithiation process, indicating the impossible regeneration of [Bi₆O₄](OH)₄(NO₃)₆·H₂O/C. At the same time, the intensity of characteristic band at 1634 cm^{−1} attributed to the bending vibration of H–O also shows slight decrease upon lithiation. During the reverse charge process, the H–O band shows no obvious evolution. These results also indicate that an irreversible phase transformation reaction from [Bi₆O₄](OH)₄(NO₃)₆·H₂O/C to LiOH.

The *ex-situ* XRD patterns obtained at the selected capacity of charge–discharge process in Fig. 8a are performed to investigate the transformation reactions of [Bi₆O₄](OH)₄(NO₃)₆·H₂O/C and Li, and the as-obtained results are presented in Fig. 8c. The pristine pattern (a) in Fig. 8c shows a lot of characteristic diffraction peaks at 10.75°, 12.44°, 22.51°, 23.22°, 25.34° and 26.32° corresponding to the characteristic lines of [Bi₆O₄](OH)₄(NO₃)₆·H₂O (JCPDS card No. 71-1360). Furthermore, the characteristic peaks at 43.24° and 50.41° can be identified to copper foil current collector (JCPDS card No. 03-1005). It can be observed that the characteristic peaks of [Bi₆O₄](OH)₄(NO₃)₆·H₂O weaken gradually during the lithiation process. Then, the characteristic peaks of [Bi₆O₄](OH)₄(NO₃)₆·H₂O disappear and a new peak can be observed at 27.30° in the middle of discharge process, corresponding to the formation of metal Bi (JCPDS card No. 85-1331). After a further discharge to 0.0 V, two new diffraction peaks can be detected at 26.95° and 22.81°, corresponding to the formation of Li₃Bi (JCPDS card No. 27-0472) and LiBi alloys (JCPDS card No. 27-0422), respectively. No other diffraction peaks, such as LiOH, LiNO₃ and Li₂O, can be observed at the end of discharge, which is similar to the amorphous

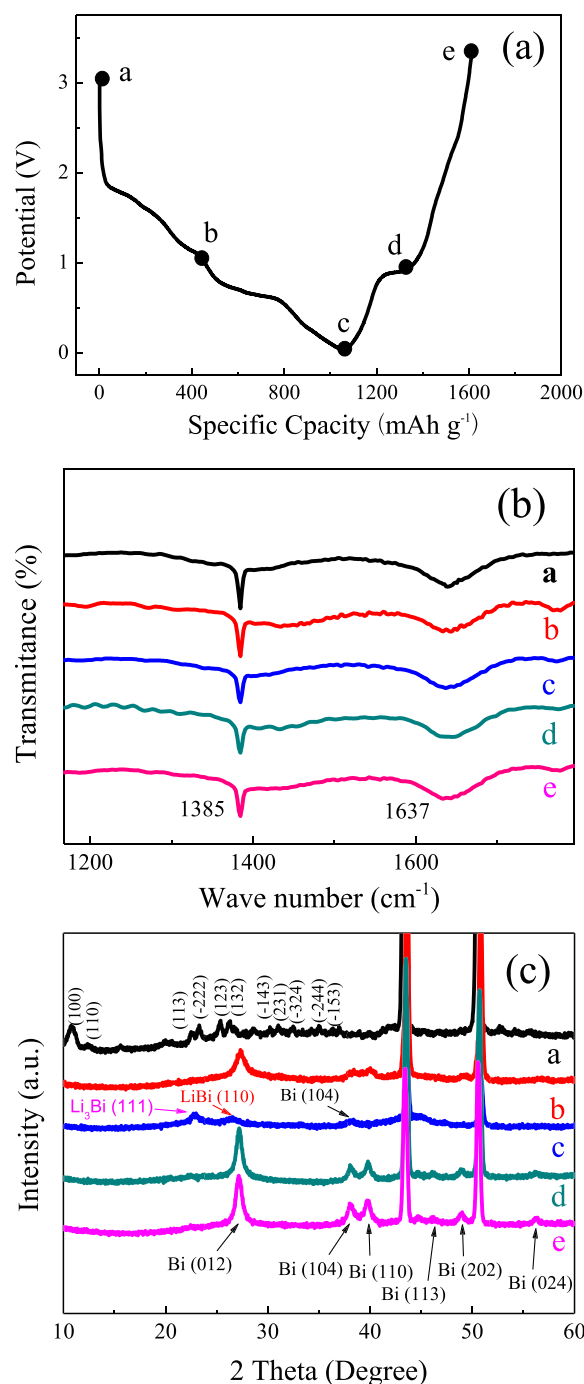


Fig. 8. Lithiated/delithiated samples (a) and corresponding *ex-situ* FTIR (b), *ex-situ* XRD (c) patterns of [Bi₆O₄](OH)₄(NO₃)₆·H₂O/C obtained for *ex-situ* XRD analysis during the initial charge–discharge process.

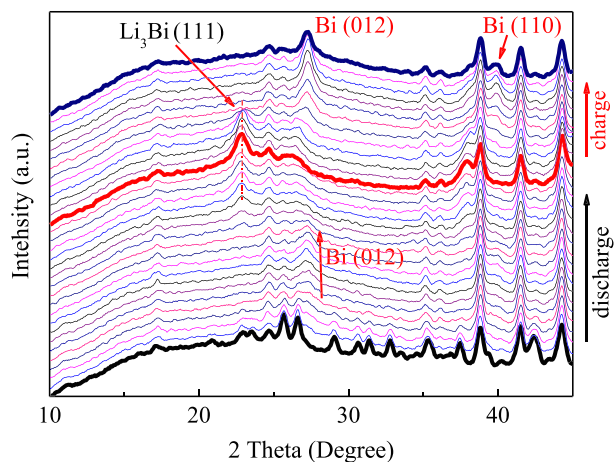


Fig. 9. *In-situ* XRD patterns of $[\text{Bi}_6\text{O}_4](\text{OH})_4(\text{NO}_3)_6 \cdot \text{H}_2\text{O}/\text{C}$ during the initial charge–discharge process.

phenomena of other metal oxides and hydroxides after full lithiation [23–25]. In the reverse delithiation process, the diffraction peaks of LiBi and Li_3Bi alloys disappear and six new diffraction peaks can be observed at 27.30° , 38.08° , 39.75° , 46.36° , 49.01° and

56.30° . These diffraction peaks are corresponding to the (012), (104), (110), (113), (202) and (024) lines of metal Bi (JCPDS card No. 85-1331). No other phases cannot be indexed to the formation of Bi_2O_3 , $\text{Bi}(\text{OH})_3$ and $\text{Bi}(\text{NO}_3)_3$. It suggests that the electrochemical reaction of $[\text{Bi}_6\text{O}_4](\text{OH})_4(\text{NO}_3)_6 \cdot \text{H}_2\text{O}/\text{C}$ with Li is partially reversible.

In order to further investigate the structural revolution of $[\text{Bi}_6\text{O}_4](\text{OH})_4(\text{NO}_3)_6 \cdot \text{H}_2\text{O}/\text{C}$ during the charge-discharge process, the *in-situ* XRD results are studied and shown in Fig. 9. Due to the use of thick Be disc (2 mm) as X-ray transmission window, some diffraction peaks in low angle range ($<20^\circ$) cannot be observed in this experiment. As shown in Fig. 9, the evolution of characteristic diffraction peaks can still be observed in the first cycle. It is clearly observed that the characteristic diffraction peaks of $[\text{Bi}_6\text{O}_4](\text{OH})_4(\text{NO}_3)_6 \cdot \text{H}_2\text{O}/\text{C}$ become weaker upon lithiation and finally disappear during the initial discharge process. The appearance of diffraction peak at 27.26° contributing to the characteristic (012) peak of metal Bi (JCPDS card No. 85-1329) can be observed during the discharge process. Upon further lithiation, this characteristic peak of metal Bi disappears and a new diffraction peak appears at 22.82° corresponding to the (111) line of Li_3Bi (JCPDS card No. 27-0472). This phenomenon is consistent with the *ex-situ* XRD result. In the reverse charge process, the diffraction peak at 22.82° becomes weaker and totally disappears. For comparison, the characteristic peaks of metal Bi appears at 27.26° and 39.84° (JCPDS card

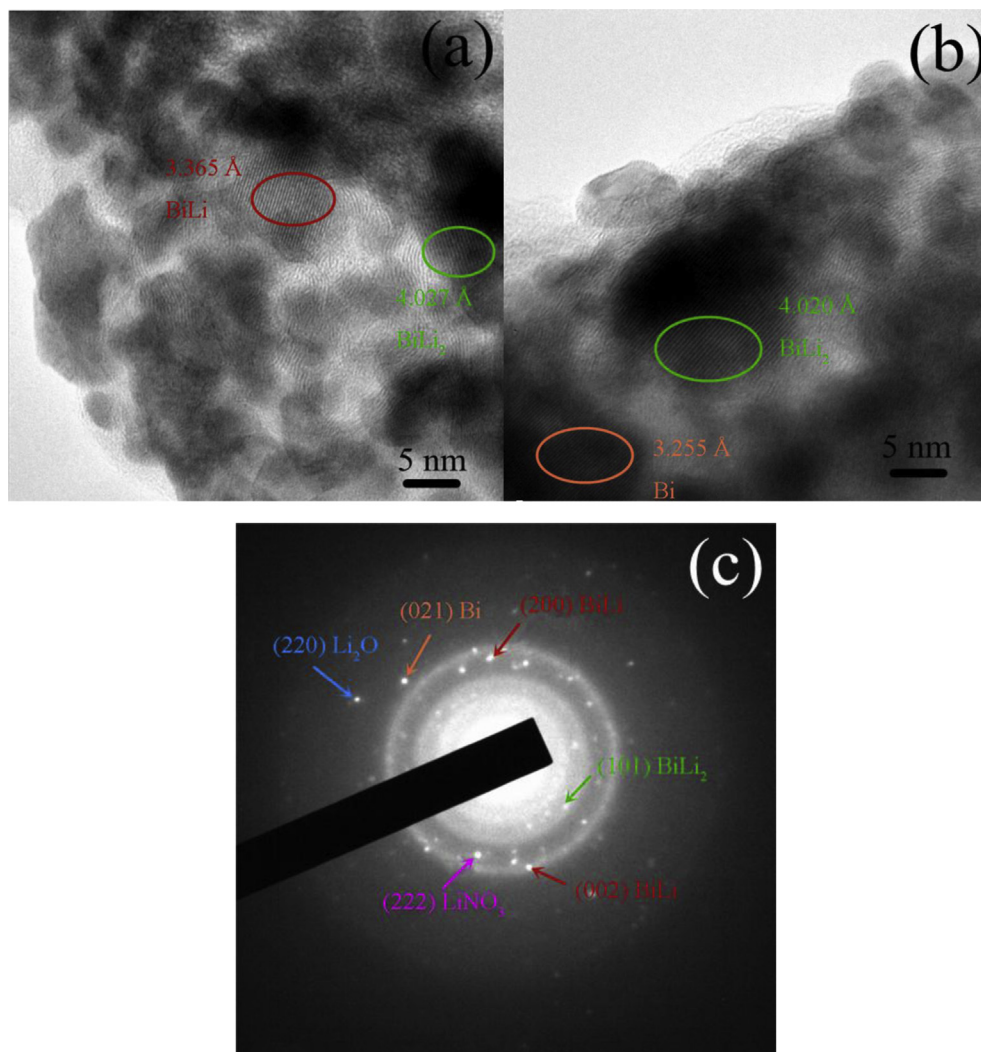


Fig. 10. (a, b) HRTEM images and (c) corresponding SAED pattern of lithiated $[\text{Bi}_6\text{O}_4](\text{OH})_4(\text{NO}_3)_6 \cdot \text{H}_2\text{O}/\text{C}$ sample after a discharge process to 0.0 V.

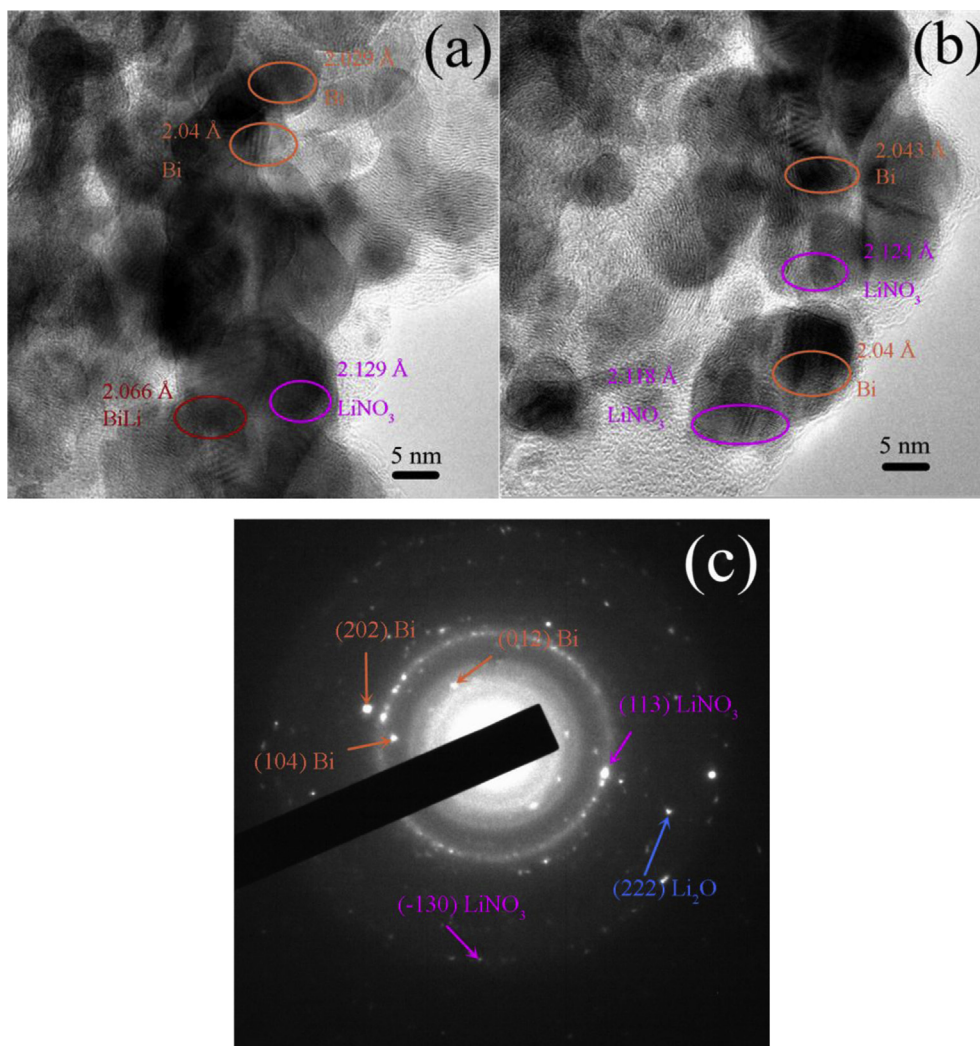


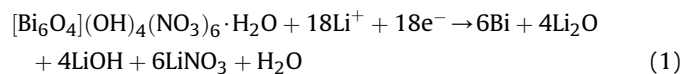
Fig. 11. (a, b) HRTEM images and (c) corresponding SAED pattern of delithiated $[\text{Bi}_6\text{O}_4](\text{OH})_4(\text{NO}_3)_6 \cdot \text{H}_2\text{O}/\text{C}$ sample after a reverse charge process to 3.4 V.

No. 85-1329), indicating the de-alloying process of Li–Bi alloys to form metal Bi during the charge process.

Figs. 10 and 11 show the *ex-situ* HRTEM and *ex-situ* SAED patterns obtained at 0.0 and 3.4 V. After a discharge process to 0.0 V, three characteristic interplanar distances can be detected in Fig. 10a, b and measured to the values of 3.255, 3.365, and 4.020 (4.027) Å, which are respectively ascribed to (012) plane of metal Bi (JCPDS card No. 85-1331), (110) plane of LiBi alloy (JCPDS card No. 27-0422) and (110) plane of Li_2Bi alloy (JCPDS card No. 45-0956). These HRTEM results are proved by the appearance of diffraction ring patterns of Bi, LiBi and Li_2Bi in Fig. 10c. Besides, the appearance of Li_2O and LiNO_3 is also confirmed by the observation of characteristic planes of (220) line (1.618 Å) for Li_2O and (222) line (2.533 Å) for LiNO_3 . The formation of metal Bi, Li–Bi alloys, Li_2O and LiNO_3 provides the evidence to confirm the electrochemical decomposition mechanism of $[\text{Bi}_6\text{O}_4](\text{OH})_4(\text{NO}_3)_6 \cdot \text{H}_2\text{O}/\text{C}$, which is also in agreement with the conclusions of *ex-situ* XRD and *in-situ* XRD observations. With a reverse charge to 3.4 V, almost all characteristic interplanar distances and ring patterns for Li–Bi alloys disappear except for the (201) plane of LiBi alloy as shown in Fig. 11. Moreover, the clear existence of characteristic interplanar distances and ring patterns for Li_2O and LiNO_3 indicates the irreversible transformation of $[\text{Bi}_6\text{O}_4](\text{OH})_4(\text{NO}_3)_6 \cdot \text{H}_2\text{O}$

into Li_2O and LiNO_3 . It also suggests that the de-alloying of Li–Bi alloys should be mainly responsible for the reverse charge capacity for $[\text{Bi}_6\text{O}_4](\text{OH})_4(\text{NO}_3)_6 \cdot \text{H}_2\text{O}/\text{C}$.

Based on the above *ex-situ* FTIR, *ex-situ* XRD, *in-situ* XRD, *ex-situ* HRTEM, *ex-situ* SAED results and previous reports about oxides, hydroxides and carbonates [13,15,23,24,26–28], the lithium storage mechanism of $[\text{Bi}_6\text{O}_4](\text{OH})_4(\text{NO}_3)_6 \cdot \text{H}_2\text{O}/\text{C}$ during the charge–discharge process can be described by the following equations:



As the *ex-situ* and *in-situ* results described in Supplementary materials, the lithium storage mechanism of $[\text{Bi}_6\text{O}_4](\text{OH})_4(\text{NO}_3)_6 \cdot 4\text{H}_2\text{O}$ is similar to that of $[\text{Bi}_6\text{O}_4](\text{OH})_4(\text{NO}_3)_6 \cdot \text{H}_2\text{O}$. Therefore, the electrochemical reaction of $[\text{Bi}_6\text{O}_4](\text{OH})_4(\text{NO}_3)_6 \cdot \text{H}_2\text{O}$

(or $[\text{Bi}_6\text{O}_4](\text{OH})_4(\text{NO}_3)_6 \cdot 4\text{H}_2\text{O}$) with Li will firstly lead to the preliminary formation of metal Bi, LiNO_3 , LiOH , Li_2O and H_2O and then result in the alloying reaction to form Li–Bi alloys. In the reverse charge process, the de-alloying of Li–Bi alloys should be responsible for the reversible lithium storage capacity in the subsequent cycles, which makes $[\text{Bi}_6\text{O}_4](\text{OH})_4(\text{NO}_3)_6 \cdot \text{H}_2\text{O}/\text{C}$ to be a promising anode materials for lithium-ion batteries.

4. Conclusions

In this paper, $[\text{Bi}_6\text{O}_4](\text{OH})_4(\text{NO}_3)_6 \cdot 4\text{H}_2\text{O}$, $[\text{Bi}_6\text{O}_4](\text{OH})_4(\text{NO}_3)_6 \cdot \text{H}_2\text{O}$ and $[\text{Bi}_6\text{O}_4](\text{OH})_4(\text{NO}_3)_6 \cdot \text{H}_2\text{O}/\text{C}$ are prepared from $\text{Bi}(\text{NO}_3)_3 \cdot 5\text{H}_2\text{O}$ and used as anode materials for lithium-ion batteries. Although $[\text{Bi}_6\text{O}_4](\text{OH})_4(\text{NO}_3)_6 \cdot 4\text{H}_2\text{O}$ electrode shows higher initial charge capacity ($1818.6 \text{ mAh g}^{-1}$) and reversible specific capacity (403.1 mAh g^{-1}) than those of $[\text{Bi}_6\text{O}_4](\text{OH})_4(\text{NO}_3)_6 \cdot \text{H}_2\text{O}$ (832.2 and 54.4 mAh g^{-1}) and $[\text{Bi}_6\text{O}_4](\text{OH})_4(\text{NO}_3)_6 \cdot \text{H}_2\text{O}/\text{C}$ (606.6 and 376.3 mAh g^{-1}) in the first 25 cycles, $[\text{Bi}_6\text{O}_4](\text{OH})_4(\text{NO}_3)_6 \cdot \text{H}_2\text{O}/\text{C}$ exhibits better cycle performance than that of $[\text{Bi}_6\text{O}_4](\text{OH})_4(\text{NO}_3)_6 \cdot \text{H}_2\text{O}$ and $[\text{Bi}_6\text{O}_4](\text{OH})_4(\text{NO}_3)_6 \cdot 4\text{H}_2\text{O}$ during long-term cycles (≥ 30). Furthermore, the capacity retention (60.3%) and reversible specific capacity (365.5 mAh g^{-1}) of $[\text{Bi}_6\text{O}_4](\text{OH})_4(\text{NO}_3)_6 \cdot \text{H}_2\text{O}/\text{C}$ are much higher than those of bare $[\text{Bi}_6\text{O}_4](\text{OH})_4(\text{NO}_3)_6 \cdot \text{H}_2\text{O}$ (4.75% and 39.6 mAh g^{-1}) and $[\text{Bi}_6\text{O}_4](\text{OH})_4(\text{NO}_3)_6 \cdot 4\text{H}_2\text{O}$ (15.9% and 289.4 mAh g^{-1}) in the first 30 cycles. The structure transformation of $[\text{Bi}_6\text{O}_4](\text{OH})_4(\text{NO}_3)_6 \cdot \text{H}_2\text{O}/\text{C}$ is also studied by *ex-situ* FTIR, *ex-situ* XRD and *in-situ* XRD techniques during the first charge–discharge cycle. The results of *ex-situ* FTIR show a asymmetrical evolution of the relative intensities of NO_3^- and $\text{H}-\text{O}$ bands, which indicates that the irreversibility of structural transformation for $[\text{Bi}_6\text{O}_4](\text{OH})_4(\text{NO}_3)_6 \cdot \text{H}_2\text{O}/\text{C}$ during the charge–discharge process. *Ex-situ* and *in-situ* XRD results show that the reversible alloying and de-alloying reaction of Li–Bi alloys should be responsible for the reversible lithium storage capacity of $[\text{Bi}_6\text{O}_4](\text{OH})_4(\text{NO}_3)_6 \cdot \text{H}_2\text{O}/\text{C}$.

Acknowledgments

This work is sponsored by National 863 Program (2013AA050901) and National Natural Science Foundation of China (No. 51104092). The work is also supported by K.C. Wong Magna Fund in Ningbo University, Open Foundation of State Key Laboratory of Materials Processing and Die & Mould Technology (2012-P01), Open Foundation of State Key Laboratory of Electronic Thin Films and Integrated Devices (KFJJ201209) and Opening Project of State Key Laboratory

of High Performance Ceramics and Superfine Microstructure (SKL201308SIC).

Appendix A. Supplementary data

Supplementary data related to this article can be found at <http://dx.doi.org/10.1016/j.jpowsour.2013.12.121>

References

- [1] M. Armand, J.M. Tarascon, *Nature* 451 (2008) 652–657.
- [2] C. Liu, F. Li, L.P. Ma, H.M. Cheng, *Adv. Mater.* 22 (2010) 28–62.
- [3] B. Scrosati, J. Garche, *J. Power Sources* 195 (2010) 2419–2430.
- [4] B.V. Ratnakumar, M.C. Smart, C.K. Huang, D. Perrone, S. Surampudi, S.G. Greenbaum, *Electrochim. Acta* 45 (2000) 1513–1517.
- [5] Y.H. Ding, J.X. Li, Y. Zhao, L.H. Guan, *Mater. Lett.* 81 (2012) 105–107.
- [6] F.F. Lin, H.H. Song, S.Q. Tian, X.H. Chen, J.S. Zhou, F. Wang, *Electrochim. Acta* 83 (2012) 305–310.
- [7] J.B. Ducros, S. Bach, J.P. Pereira-Ramos, P. Willmann, *Electrochim. Acta* 52 (2007) 7035–7041.
- [8] Q. Sun, Z.W. Fu, *Appl. Surf. Sci.* 258 (2012) 3197–3201.
- [9] B.N. Hu, X.Y. Wang, Y.P. Wang, Q.L. Wei, Y.F. Song, H.B. Shu, X.K. Yang, *J. Power Sources* 218 (2012) 204–211.
- [10] B.A. Hu, X.Y. Wang, H.B. Shu, X.K. Yang, L. Liu, Y.F. Song, Q.L. Wei, H. Hu, H. Wu, L.L. Jiang, X. Liu, *Electrochim. Acta* 102 (2013) 8–18.
- [11] L. Liu, X.Y. Wang, X.Y. Wang, X. Wang, F.H. Tian, L.H. Yi, *Electrochim. Acta* 56 (2011) 7437–7441.
- [12] Y.N. NuLi, J. Yang, M.S. Jiang, *Mater. Lett.* 62 (2008) 2092–2095.
- [13] C.M. Park, S. Yoon, S. Lee, H.J. Sohn, *J. Power Sources* 186 (2009) 206–210.
- [14] Z.A. Zhang, C.K. Zhou, H. Lu, M. Jia, Y.Q. Lai, J. Li, *Mater. Lett.* 91 (2013) 100–102.
- [15] H. Jung, C.M. Park, H.J. Sohn, *Electrochim. Acta* 56 (2011) 2135–2139.
- [16] Z. Ali, C.B. Cao, J.L. Li, Y.L. Wang, T. Cao, M. Tanveer, M. Tahir, F. Idrees, F.K. Butt, *J. Power Sources* 229 (2013) 216–222.
- [17] B. Das, M.V. Reddy, P. Malar, T. Osipowicz, G.V.S. Rao, B.V.R. Chowdari, *Solid State Ionics* 180 (2009) 1061–1068.
- [18] Q. Sun, W.J. Li, Z.W. Fu, *Solid State Sci.* 12 (2010) 397–403.
- [19] Q. Sun, Z.W. Fu, *Electrochem. Solid-State Lett.* 10 (2007) A189–A193.
- [20] D. Aurbach, I. Weissman, A. Zaban, P. Dan, *Electrochim. Acta* 45 (1999) 1135–1140.
- [21] C. Burns, N.N. Sinha, G. Jain, H. Ye, C.M. VanElzen, E. Scott, A. Xiao, W.M. Lamanna, J.R. Dahn, *J. Electrochem. Soc.* 160 (2013) A2281–A2287.
- [22] K. Vivekanandan, S. Selvasekarapandian, P. Kolandaivel, *Mater. Chem. Phys.* 39 (1995) 284–289.
- [23] S.B. Ni, X.H. Lv, T. Li, X.L. Yang, L.L. Zhang, *J. Mater. Chem. A* 1 (2013) 1544–1547.
- [24] Y.S. He, D.W. Bai, X.W. Yang, J. Chen, X.Z. Liao, Z.F. Ma, *Electrochem. Commun.* 12 (2010) 570–573.
- [25] P. Poizot, S. Laruelle, S. Grugeon, L. Dupont, J.M. Tarascon, *Nature* 407 (2000) 496–499.
- [26] J.C. Perez-Flores, A. Kuhn, F. Garcia-Alvarado, *J. Power Sources* 182 (2008) 365–369.
- [27] L.W. Su, Z. Zhou, X. Qin, Q.W. Tang, D.H. Wu, P.W. Shen, *Nano Energy* 2 (2013) 276–282.
- [28] L.Y. Shao, J. Shu, R. Ma, M. Shui, L. Hou, K.Q. Wu, D.J. Wang, Y.L. Ren, *Int. J. Electrochem. Sci.* 8 (2013) 1170–1180.